Appl. Phys. A 66, S659–S667 (1998)

Applied Physics A
Materials
Science & Processing

AFM-tip-induced and current-induced local oxidation of silicon and metals

Ph. Avouris*, **R. Martel, T. Hertel, R. Sandstrom**

IBM Research Division, T.J. Watson Research Center, Yorktown Heights, USA

Received: 25 July 1997/Accepted: 1 October 1997

Abstract. Here we discuss two different processes that can be used to locally oxidize silicon or metals and are promising for the fabrication of model nanoelectronic devices. The first involves oxidation induced by a negatively biased conducting atomic force microscope (AFM) tip. We examine the kinetics and mechanism of this process and how factors such as the strength of the electric field, thickness of the oxide, and ambient humidity affect its rate and resolution. Weak ionic currents are detected, pointing to the electrochemical character of the process. Very fast initial oxidation rates are found to slow down dramatically as a result of the build up of stress and the reduction of the electric field strength. The lateral resolution is found to be largely determined by the defocusing of the electric field by a water film, surrounding the tip, whose extent is a function of ambient humidity. The second approach involves local oxidation induced by high current densities generated by forming constrictions in the current-carrying sample. This novel local oxidation process can be used to generate thin oxide tunneling barriers of 10–50 nm.

Microelectronic devices have reached a stage of great sophistication and perfection. It is, however, clear that the continuous improvements to which we have been accustomed for several decades will eventually come to an end if we limit ourselves to the current device concepts. Thus, it has become important to find new device principles that would allow us to continue the process of miniaturization and integration well into the 21st century. The perturbations the tips of proximal probe microscopes (STM&AFM) induce to the surface of a solid have been used to produce structural or chemical modifications of materials [1–3]. The simplicity and low cost of the approach has generated interest in developing it as a fabrication process of model nano-electronic devices whose function is to be assessed. Among the various modification schemes explored so far the most promising appears to be the process of tip (field)-induced oxidation. Using this process, one can generate oxide patterns on semiconductors or metals. Unlike most other modifications produced by proximal probes, the structures produced with this approach are three-dimensional. The size (line-width) of the structures produced is in the range of a few to tens of nanometers. This is the next relevant size range for electronic devices; devices significantly smaller than that would face great problems of stability and fabrication and are not likely to become important for some time to come. One of the problems associated with very small conducting structures is their instability brought about, primarily, by the high current densities that develop in them. Although these current densities usually lead to the destruction of the structures, here we demonstrate that the effects of high current densities can be controlled to produce desirable structural and chemical modifications of materials on the nanometer scale.

The earliest report of tip-induced oxidation was by Dagata et al. [4]. These workers oxidized silicon by scanning H-passivated Si in air with a positively biased STM tip. Other workers used a different approach in which the sample is scanned by a negatively biased tip [5–11]. Instead of an STM, an AFM with a conducting tip is usually employed so that the process can be used to produce thicker, non-conducting oxides. This approach has also been used to fabricate simple device structures [12–15]. However, the mechanism of the process and the factors that control its rate and resolution remain unclear. The fact that water vapor in the ambient environment is necessary was considered by Sugimura et al. [11] as an indication that the oxidation reaction may be analogous to electrochemical anodization. No electrochemical current has been detected, however. Here we study the dependence of the reaction rate on the electric field strength and oxide thickness and determine the factors that control the depth and the lateral extent of the oxide patterns, i.e. the resolution of the process [16].

In the second part of the paper we show that local nanochemistry can be induced by the action of high electric current densities flowing through thin metal films in air.

* E-mail: avouris@us.ibm.com

Specifically, ultra-thin (10–50 nm) metal/oxide tunneling barriers can be fabricated in a self-limiting way and in any desired position simply by making constrictions of the current path using the AFM oxidation process. The electrical characteristics of the resulting oxide barriers are determined, and the possible mechanism of the process is discussed.

1 Experimental

The samples used in the oxidation experiments were n-type (8–12 Ω cm) Si(100) wafers. The native oxide was removed using an aqueous 10% HF solution. Local oxidation was performed in the ambient with conducting p^{++}-Si tips (radius < 100 Å) and a computer controlled commercial AFM microscope (M5, Park Scientific Instruments). The relative humidity was kept constant during experiments at values ranging from 10%–95%. AFM measurements of line widths involve a convolution with the tip shape. Metal thin films were deposited on Si(100) wafers covered with 130 nm of SiO_2 by using dc magnetron or electron beam evaporation. Patterning of the metal films was accomplished with optical lithography employing a Karl Suss aligner. Contact pads made of Al(+4% Cu) were also fabricated by using lithographic techniques. Electrical measurements were performed with a precision semiconductor parameter analyzer (HP model 4156A).

2 AFM Tip-induced oxidation

2.1 Oxidation kinetics

Figure 1 (top) gives an example of patterned oxidation of silicon with an AFM tip. Given the different chemical properties of the oxide, subsequent chemical reactions can be used to produce patterns of different composition. For Fig. 1 (bottom) aqueous HF was used to preferentially etch the oxide.

One of the most important pieces of information needed in considering the use of this oxidation process in fabrication is its intrinsic rate. The study of the reaction kinetics is also essential for elucidating the mechanism of the oxidation process. To determine the reaction kinetics, we applied voltage pulses with the tip stationary over a surface site. The applied voltage could be varied between -2 V and -20 V and the pulse duration was increased from 10 ms to 1000 s while the tip was moved to a new position before each pulse. The width and height of the resulting oxide dots was obtained from AFM images (see Fig. 2, top). To obtain the total amount of Si oxidized, we also imaged the indentations left after the oxide was selectively etched away by aqueous HF (Fig. 2, bottom). In this way, we found an apparent volume expansion upon oxidation of 3.0 ± 0.4, which is higher than the anticipated increase of 2.3 for formation of amorphous SiO_2.

Kinetic measurements are shown in Fig. 3 where the height of the oxide dots under the tip apex is plotted as a function of the voltage pulse duration t. The fits to the data show a rapid decrease of the growth rate with time as $1/t$. No clear bias threshold was observed. For sufficiently long pulses shallow oxides were grown with a tip bias as low as -2 V.

The bias dependence of the rate indicates that the electric field plays an important role in the oxidation process. Very high initial growth rates are observed at extreme electric field strengths near the tip apex of up to $\sim 10^8$ V/cm. In estimating the field we have assumed that the entire voltage drop takes place across the oxide. Field enhanced oxidation was first modeled theoretically by Cabrera and Mott [17]. In their model, the role of the electric field is to lower the activation barrier for transport of ionic species across the oxide. The decrease of the growth rate observed here would then be attributed to the reduction of the electric field strength as the oxide thickness increases. To confirm the involvement of ionic species in the tip-induced oxidation process we searched for the very weak (femto-ampere) Faraday currents expected. The measured current in Fig. 4 shows the same time evolution as the expected Faraday current calculated from the experimentally measured volume growth and by taking into account that four elementary charges are need to oxidize one Si atom. The charge efficiency obtained from the comparison of the observed and calculated results is $\sim 50\%$.

Using the straight line fits of the kinetic data in Fig. 3 we can obtain the growth rate as a function of the electric field strength at the tip apex (Fig. 5). The high initial rates ($\sim 10^3$ Å/s for -20 V) decrease quickly with decreasing electric field strength and we find that the oxide practi-

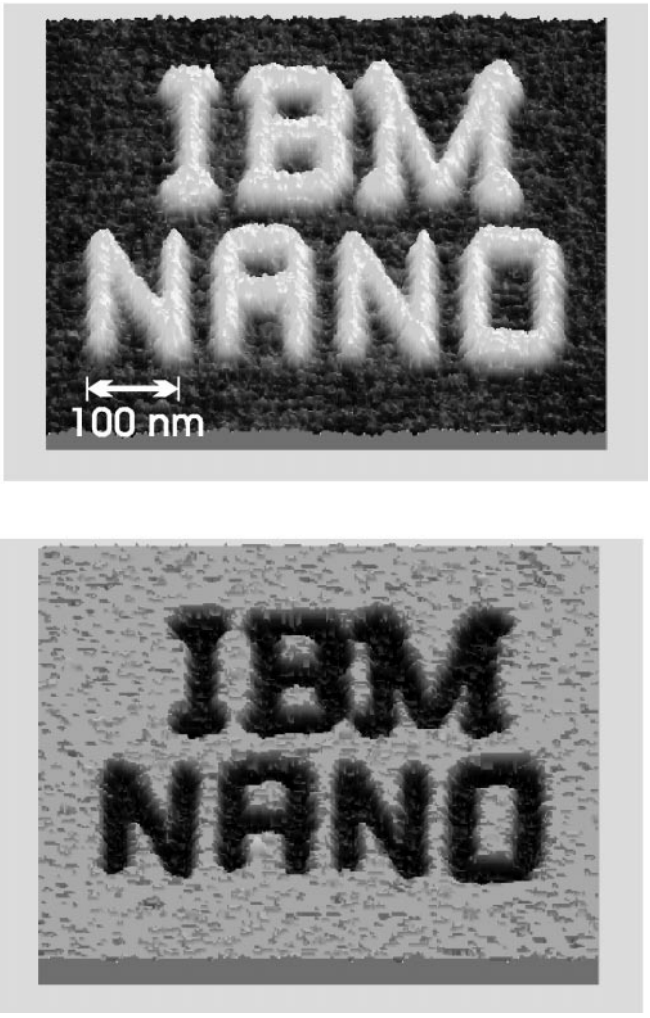

Fig. 1. *Top*: AFM-tip-induced oxide pattern on Si(100). Tip bias -10 V. *Bottom*: After etching the oxide for 15 s using 50:1 aqueous HF solution

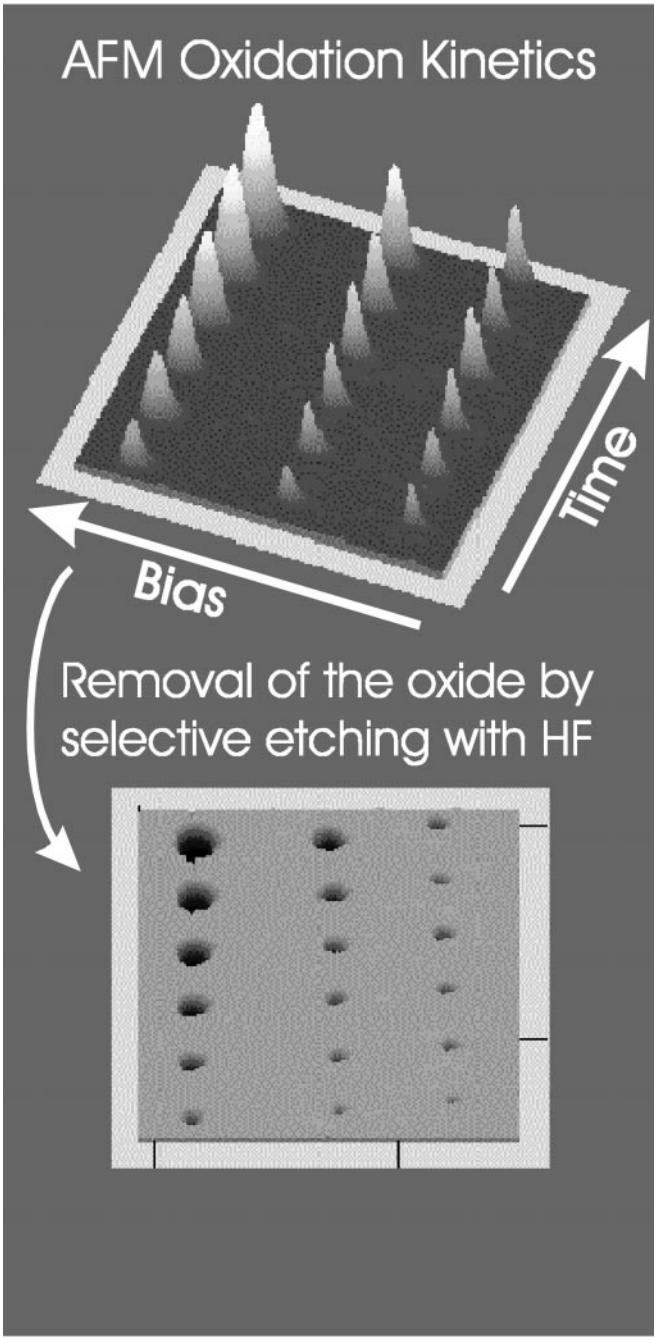

Fig. 2. Illustration of the use of AFM to study the kinetics of tip-induced oxidation

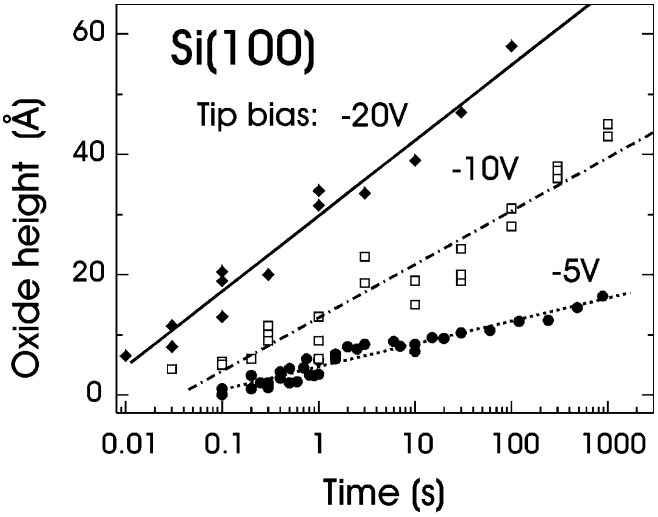

Fig. 3. Kinetics of oxide dot growth for different tip biases at ~ 50% ambient humidity

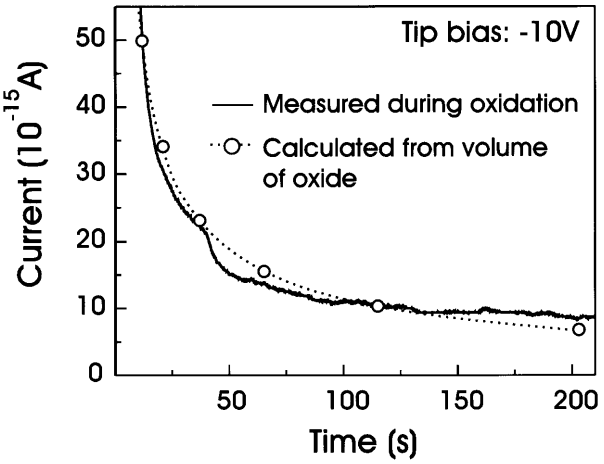

Fig. 4. Current detected during tip-induced oxidation. Dots indicate current calculated on the basis of measured oxide volume (see text)

cally stops growing at field strengths $< 1 \times 10^7$ V/cm. It is also clear from Fig. 5 that the oxidation rate is not only a function of electric field strength but also depends on the applied bias.

More insight on the factors that affect the oxidation kinetics is obtained by plotting the oxidation rate, $\mathrm{d}x/\mathrm{d}t$, as a function of the oxide thickness, x. Figure 6 shows that the rate falls off exponentially with x according to $\mathrm{d}x/\mathrm{d}t \propto \exp(-x/L)$, where L is a characteristic length that depends on the applied bias. The observed behavior is not compatible with the simple Cabrera–Mott model where the rate is proportional to $\exp(qa\Delta\Phi/2xkT)$. Here, q is the charge of the transported ions, a gives the distance between interstitial sites of ions, $\Delta\Phi$ is the potential drop across the oxide, and x the oxide thickness.

An exponential dependence of the oxidation rate on oxide thickness at the early stages of oxidation has also been observed in the case of thermal oxidation (see for example [18]). It is believed that the development of stress during oxidation causes the observed thickness dependence of the oxidation rate [19, 20]. The molecular volume of SiO_2 is 45 Å^3 and that of Si is only 20 Å^3. It is this doubling in volume which is responsible for the development of stress. New oxide formed at the Si/oxide interface must push against the already formed oxide. This would lead to an additional activation energy which can be written as $\Delta E_A = -\sigma_R\,[V(SiO_2) - V(Si)]$, where σ_R is the component of stress along the growth direction. In fact not only the interface reaction, but also the other elementary processes that lead to the formation of the oxide, i.e. reactant solution and diffusion through the growing oxide, would be affected in the same way by stress as they too involve an increase in volume in the transition state. In the absence of relaxation processes, the stresses would be enor-

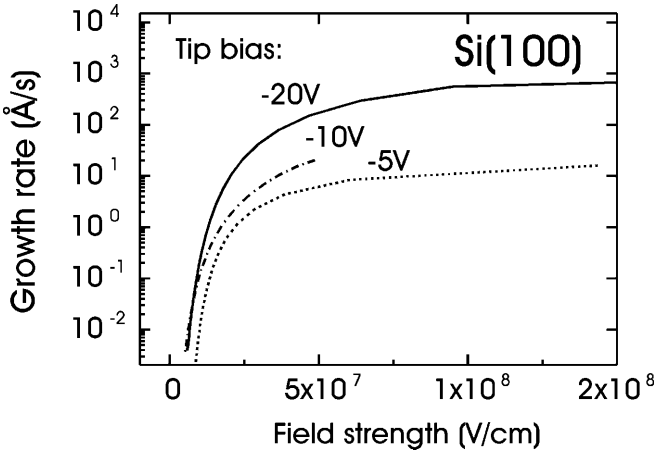

Fig. 5. Oxide growth rate as a function of the electric field strength at the tip apex

mous, of the order of 10^{12}–10^{11} dyn/cm^2 [19]. In thermal oxidation the temperature is usually high enough to allow the viscous flow of SiO_2 [20]. For example, Massound et al. [18] report that the characteristic length L increases from 4–7 Å at 800 °C to 10–20 Å at 950 °C. The AFM-induced oxidation takes place at room temperature and, therefore, no viscous flow can take place. We do, however, observe that the characteristic length increases with increasing field strength (see Fig. 6): $L = 4$ Å (at -5 V), $L = 9$ Å (-10 V), and $L = 13$ Å (-20 V). Thus, the increasing electric field seems to act like an increased temperature to counteract the stress. Possible field-dependent stress-relief mechanisms may involve silicon out-diffusion through the oxide with reaction occurring at the oxide–gas interface, or defect formation in the oxide. The observed discrepancy between the measured and expected volume expansion may be an indication that stress relief involves the formation of a rather open and defect-rich oxide.

The logarithmic dependence of the oxide height on time (Fig. 3) and the observed exponential decrease of the oxidation rate with increasing oxide thickness, x, (Fig. 6) suggest an oxide thickness dependence of the activation energy, E_A. The above results are consistent with a simple linear dependence of the form [22] $E_A(x) = E_A(0) + [E_A(\infty) - E_A(0)]\,x/L$, then the rate equation will be given by

$$\frac{dx}{dt} = R(\infty)\,e^{C} \exp\left[-C\frac{x}{L}\right] \tag{1}$$

where $R(\infty)$ is the asymptotic rate, and $C = (E_A(\infty) - E_A(0))/kT$. The solution of this equation gives a logarithmic dependence of x on time:

$$x(t) = \frac{L}{C} \ln\left[1 + \frac{C}{L}\left(x(0) + R(\infty)\,e^{C}t\right)\right] \tag{2}$$

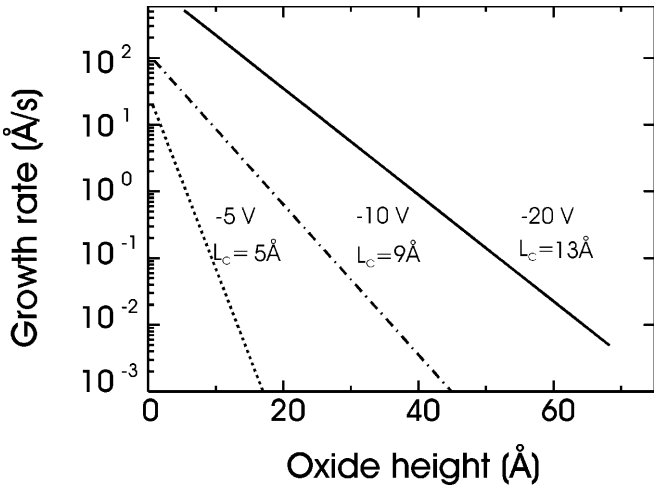

Fig. 6. Oxide growth rate as a function of oxide height at three tip biases

2.2 Lateral resolution of the oxidation process

We now address the issue of the lateral resolution of the tip-induced oxidation. Figure 7a shows the profile of an oxide dot grown at a tip bias of -10 V and an ambient humidity of 55%. The strong field dependence of the oxidation kinetics, together with the anticipated focusing of the electric field at the tip apex (radius of curvature < 100 Å) should, in principle, yield very narrow oxide structures, much narrower than that seen in Fig. 7a. Furthermore, the increase of oxide height in Fig. 7a is nearly constant over the whole dot. By calculating the electric field strength required to obtain this growth rate we find that the field strength across the oxide must be roughly constant even at large distances from the tip. This contradicts the expected field distribution from the tip in front of a conducting surface in vacuum (Fig. 7b). This field should decay approximately inversely proportionally with the distance from the tip. We attribute the observed discrepancy to the finite electrical conductance of the water film that forms between the hydrophilic oxidized regions of the surface and

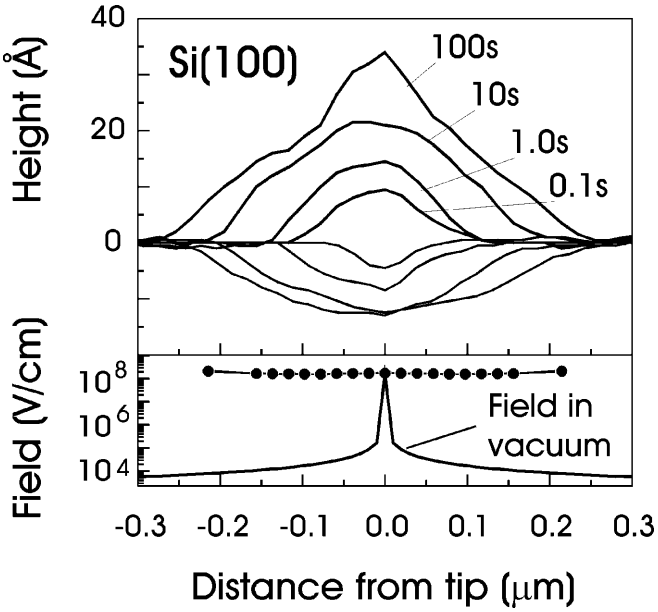

Fig. 7. a Profiles of oxide dots grown when a -10 V bias was applied to the tip for the indicated time periods. **b** The calculated electric field for a tip 30 Å in front of a conducting surface in vacuum (*solid line*) and the field calculated from the observed growth rate (*solid circles*)

the tip apex. We obtained direct evidence for the presence of such a film by obtaining force vs. distance curves on clean H/Si sites and on pre-oxidized sites (not shown). The formation and extent of the water film which "defocuses" the electric field is governed by a number of factors that include capillary forces, high electric field gradients near the tip apex, the wetting behavior of the substrate and tip, as well as the ambient humidity. The dependence of the oxidized volume on the ambient humidity at constant voltage (-10 V) and reaction time (20 s) is shown in Fig. 8a. Figure 8b shows two grids of oxide lines written with the same bias (-10 V) but at two different humidities: 61% and 14%. In this case the decrease in humidity leads to a reduction of the oxide line width by about a factor of 4.

Using the finding that the field is constant across the dot while the oxide thickness decreases linearly with the distance from the tip apex, we can obtain information about the structure of the water film around the tip. By relating current and potential drop to the resistivity of the film we find that its thickness, d, as a function of the distance from the apex, r, is given by $d(r) \propto (r_{\max}^2 - r^2)/r$, where $r_{\max}$ is the radius of the outer boundary of the water film. Finally, we note that the stress that develops during oxidation, as we discussed above, also favors oxide structures with low curvature, that is shallow oxides, because $\sigma \propto 1/R_C^2$, where R_C is the radius of curvature. Thus, both humidity and stress control the aspect ratio of the oxide structures.

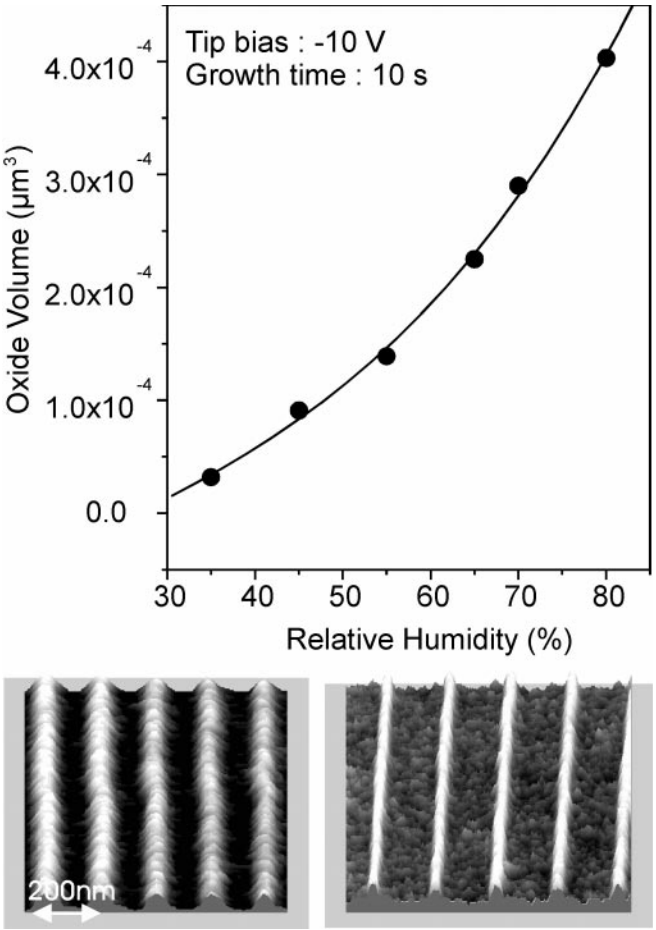

Fig. 8. *Top*: Volume of oxidized silicon as a function of ambient humidity. Tip bias $= -10$ V, reaction time $= 20$ s. *Bottom*: Two grids of oxide lines written using a tip bias of -10 V and ambient humidity of 61% (left) and 14% (right)

2.3 Oxide growth at high bias

In addition to the lateral resolution with which oxide can be grown, we need to know how thick an oxide film can be generated with the AFM. From the above discussion it would appear that by simply raising the applied bias we could grow increasingly thicker oxides, albeit with a worsening aspect ratio. However, this is not the case. At high bias (> 10 V) a new channel opens up in the oxidation mechanism. The strong electric fields present inject electrons into the conduction band of the growing oxide film. The accelerated ("hot") electrons can now generate secondary electrons. This results in avalanches that are of a stochastic nature. Evidence for their growing importance as the bias is increased is provided by both electrical measurements and oxide chemistry. Figure 9 shows a current vs. time plot (tip bias -20 V). Current spikes that tend to cluster in the earlier times are clearly evident. The fragmentation and ionization produced by the avalanches generates an abundance of reactive species that lead to fast oxidation. These localized fast reaction pathways can be seen as oxide spikes or after HF etching as localized depressions. Figure 10 shows an oxide line written at a tip bias of -20 V and subsequently etched by HF. For the most part an ~ 20 Å deep channel is formed. However, in places where presumably breakdown has occurred, deep dark-appearing holes are formed. Line scans show that the depth of the holes can be more than twice that of the channels formed by the anodic oxidation process. This avalanche induced component of the chemistry limits the magnitude of the bias that can be applied and, therefore, the thickness of a uniform oxide film that can be formed by the AFM oxidation process.

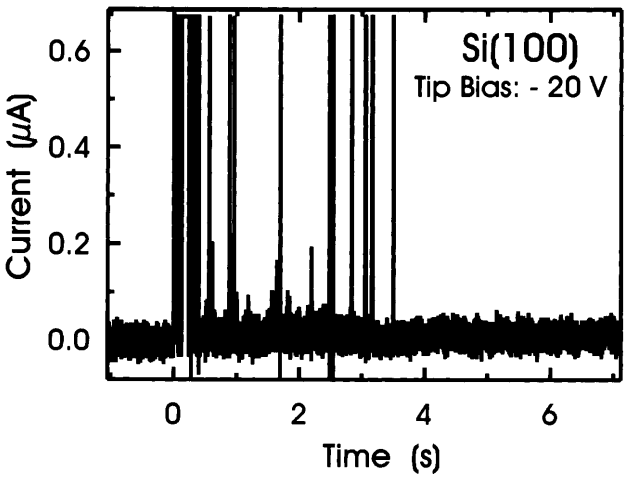

Fig. 9. Current as a function of time after switching on a -20 V bias on AFM tip

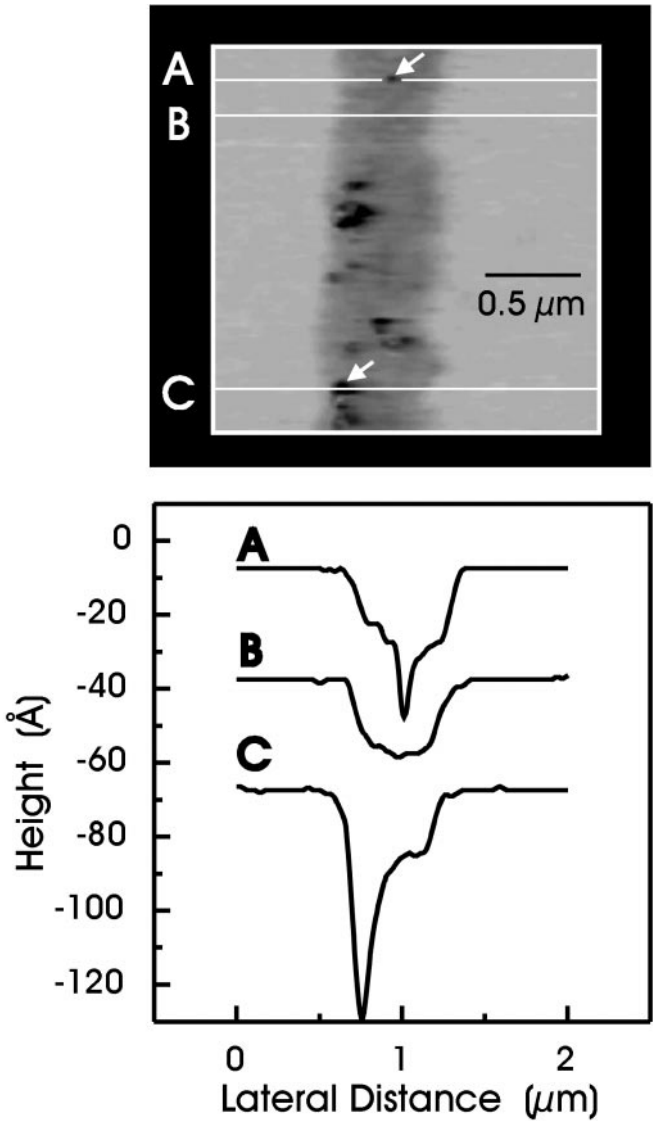

Fig. 10. *Top*: Trench produced by oxidizing Si(100) with a tip at −20 V and subsequently etching the oxide with aqueous HF. *Bottom*: Line scans across the trench

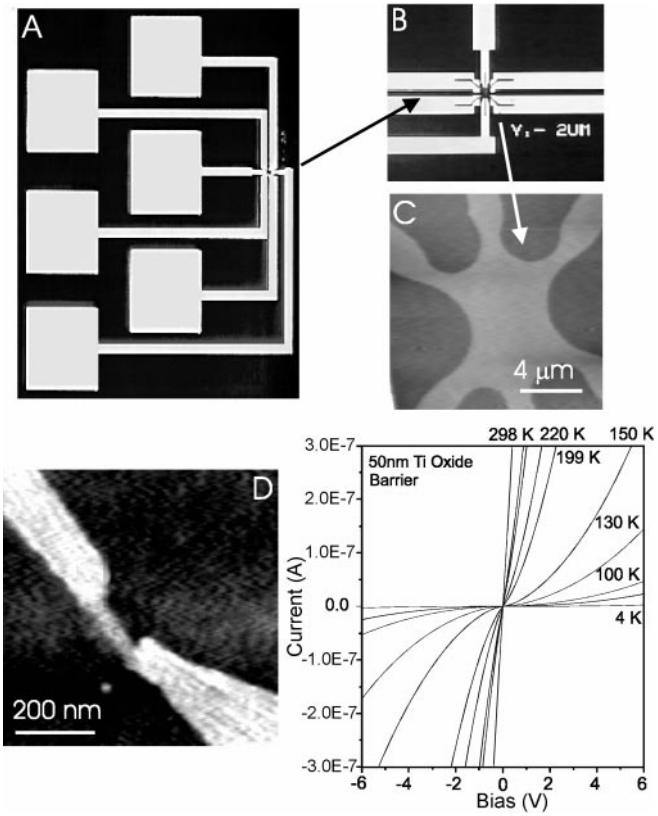

Fig. 11. a Lithographically defined electrical pad structure. **b** and **c** close-ups of the active area showing a star-like pattern made of a 3-nm-thick Ti film on an insulating SiO_2 substrate. **d** Oxide barrier fabricated on one of the side arms of the Ti star pattern with the AFM tip. **e** Current–voltage (I–V) characteristics of the oxide tunnel barrier as a function of temperature

2.4 Oxide electrical properties

In contemplating future electronic devices in the size range of only a few nanometers, we quickly realize that two kinds of materials are relevant: conductors and insulators. Semiconductors that form the basis of modern microelectronics lose their importance because of problems associated with the difficulty of doping such small structures. For example, the maximum dopant concentration in silicon is in the range of 10^{19} dopant atoms/cm^3. Even at that concentration the average distance between dopants is ~ 4.5 nm. Thus, statistical fluctuations in the dopant concentration become exceedingly important and problematic in nanodevices. Most of the proposed schemes for new quantum electronic devices involve the confinement of electrons by using tunneling barriers and the modification of their energies by using gates [23]. The AFM-induced oxidation process is well suited for the fabrication of such devices as it is able to generate in situ patterns involving conductors and insulators. By choosing the nature of the conductor to be oxidized one can tune the tunneling barrier height. For example, by oxidizing metals such as Nb, Ti or Cr oxide barriers with heights of 100–300 meV are created, whereas high barriers can be formed by, for example, oxidizing Al (1.8 eV) or Si (3 eV).

To be able to measure the electrical (transport) characteristics of AFM-fabricated nanostructures we need to provide good electrical contacts with the measurement devices. Figures 11A-C show pictures of the lithographically defined work area. It involves a star-like pattern of a very thin Ti film (~ 3 nm) on an insulating film of SiO_2 in contact with Al pads. AFM-induced oxidation can oxidize the film down to the SiO_2 insulator. Figure 11D, shows a tunneling barrier generated in one of the side arms of the star pattern, and Fig. 11E shows the current–voltage (I–V) characteristics of this structure as a function of temperature. The non-ohmic character of the transport is clearly evident. Transport takes place by thermal activation over the barrier and tunneling through the barrier. Analysis of the temperature dependence of the current allows the determination of the barrier height (see Sect. 3).

3 Current-induced oxidation

The high current densities that can be generated with the STM have been shown to lead to interesting new chemistry involving the breaking of chemical bonds via a multiple-

vibrational excitation mechanism [24]. Here we show that the high electric current densities that can be generated inside nanowires and nanoconstrictions can also lead to local chemistry. The reaction rate is again a strong function of the current density and this leads to nanometer scale spatial resolution. It is known that an electric current flowing through a conductor exerts forces on defect atoms in the conductor [25]. Usually, two types of forces are distinguished. One, the so-called electron wind force, results from the momentum transfer in electron–atom collisions. The direction of this force is the same as that of the electron flow, and its magnitude is $F_{\mathrm{EW}} \propto J_{\mathrm{e}} \propto \varrho E$, where J_{e} is the electron current density and σ the conductivity. The other force is the result of the electric field acting directly on the nominal charge (ze) of the atom, i.e. $F_{\mathrm{EF}} = zeE$, and has the opposite direction to F_{EW}. In most cases $F_{\mathrm{EW}} > F_{\mathrm{EF}}$ and the atoms move in the same direction as the electrons. The resulting net atomic current can be written as [25]

$$J_{\mathrm{A}} \propto \frac{NJ_{\mathrm{e}}}{kT}\left[D_0 \exp(-W_{\mathrm{D}}/kT)\right] \tag{3}$$

where N is the number of the atoms, and D_0 and W_{D} are their diffusion coefficient and diffusion activation energy, respectively. From (3) we see that electric-current-induced atomic motion, so-called electromigration, becomes important at high electron current densities or electric fields. Along with the atomic current we can consider that a vacancy current J_{V} is formed and moves in the opposite direction. Joule and local heating effects further increase the atom/vacancy currents. Permanent structural changes occur at places where the divergence of the current is not zero, i.e. $\nabla J_{\mathrm{A,V}} \neq 0$. Such locations act as sources or sinks of atoms. The atom/vacancy current is a function of several other variables such as the local composition or the temperature, and the continuity equation $\nabla J_{\mathrm{A,V}} = -\partial N/\partial t$ suggests that the sites of local modification will be places where the gradients of these variables are large. Grain boundaries where the mobility of the atoms and the above gradients are the highest, form the preferred sites for structural modification [25]. The thin metal films we use in the oxidation experiments are nanocrystalline with an average grain size of only a few nanometers.

In our studies we found that destruction by electromigration of the our thin metal films takes place at current densities of $\sim 10^8\,\mathrm{A/cm^2}$. To induce local nanochemistry we must generate current densities of $10^7\,\mathrm{A/cm^2}$. Under these conditions current-induced atomic rearrangements can still take place. In particular, vacancy aggregation at grain boundaries creates nanocracks that act as channels that allow oxidants (O_2, H_2O) from the ambient to reach the interior of the film. The large field gradients present at grain boundaries help in this transport. Finally, Joule and local heating are also maximized at these locations and help activate the chemical reactions.

A test of the possibility of using high local current densities to induce nanochemistry is shown in Fig. 12. The structure used is the side arm of a Ti star-shaped film similar to that shown in Fig. 11. To select the place where we want the chemistry to take place, we use AFM oxidation to generate two oxide notches that constrict the current path at that location. The constriction shown in Fig. 12A has a width of $\sim 140\,\mathrm{nm}$. By applying a voltage bias of 2 V ("stress voltage") we generate a current density of $\sim 5 \times 10^7\,\mathrm{A/cm^2}$. Under these conditions, we find that in a short period of time a barrier is formed that bridges the constriction as shown in Fig. 12B. In this case, the width of the barrier convolved with the tip width is 28 nm. We have produced widths as low as 10 nm in this manner. For a given constriction, the barrier width is a function of the applied stress voltage. An example is shown in Fig. 12C. The strongly non-linear I–V (MIM diode behavior) obtained after stressing a 150 nm constriction at a voltage of 5 V is shown in Fig. 13A. By plotting the current as a function of $1/T$ one can obtain the effective tunneling barrier height $\Phi_{\mathrm{B}}^{\mathrm{eff}}$. This height is a function of the electric field and is given by $\Phi_{\mathrm{B}}^{\mathrm{eff}} = \Phi_{\mathrm{B}}^{0} - e(eE/4\pi\varepsilon_0\varepsilon)^{1/2}$, where the second term accounts for the reduction of the barrier by the electric field and by image effects. To obtain the field free value Φ_{B}^{0} we plot $\Phi_{\mathrm{B}}^{\mathrm{eff}}$ as a function of $\sqrt{E}$ and extrapolate to $E = 0$. Figure 13B shows this plot. The field-free value of the barrier height is 0.24 eV, which is very close to the value 0.28 eV reported for the Ti oxide produced by tip oxidation [14]. This result and the observation that no barrier is formed when the film is stressed in the absence of the ambient indicate that the barrier is formed by the oxidation of Ti. A measure of the oxidation rate is provided by the time evolution of the conductance. Figure 14 shows the behavior of the conductance of a 140-nm constriction during current-induced oxidation. Initially the rate of change of the conductance is slow but as the cross section of the unoxidized part of the constriction decreases, the current density increases and the oxidation rate becomes very high. This observation indicates that the rate is a strong function of the current density. This nonlinear dependence of the rate on current density is analogous to the behavior observed for hydrogen desorption induced by STM-tip-emitted electrons [24]. In both cases the strong dependence of the rate on current density tends to localize the

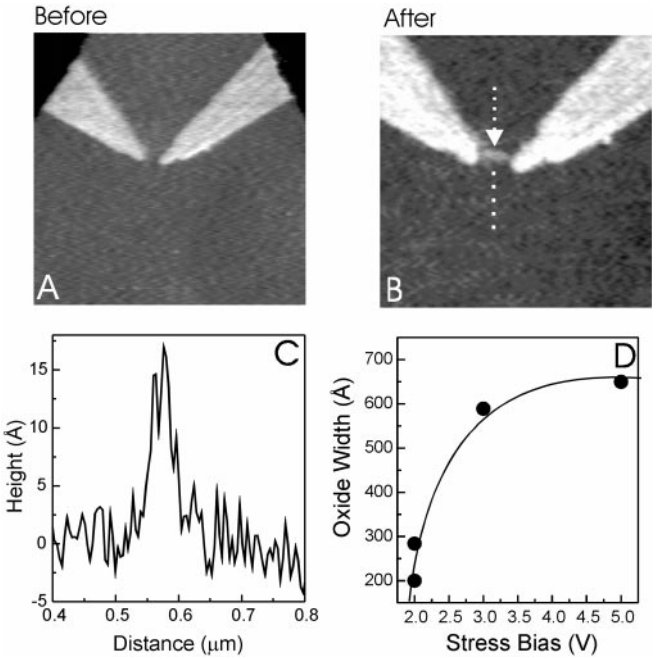

Fig. 12. **a** AFM fabricated oxide constriction on a 3-nm-thick Ti film. **b** After stressing by applying a 2-V bias a 28-nm oxide barrier is formed. **c** Line scan through the current-grown oxide. **d** Dependence of the oxide barrier width on the stress voltage

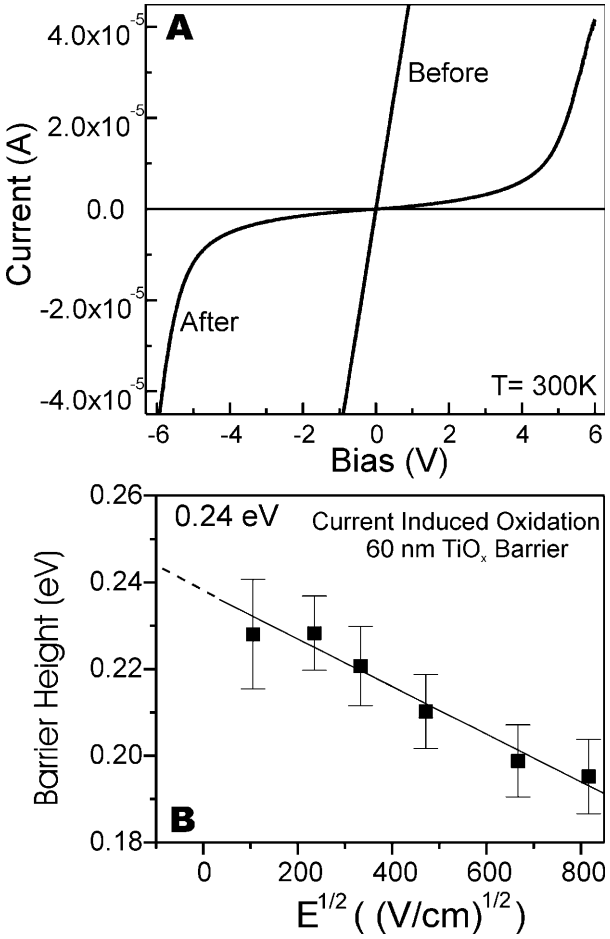

Fig. 13. *Top*: *I–V* curves before and after a 5-V stress of a 150-nm constriction on a 4-nm-thick Ti film. *Bottom*: Determination of the field-free value of the tunneling barrier generated by the 5-V stress

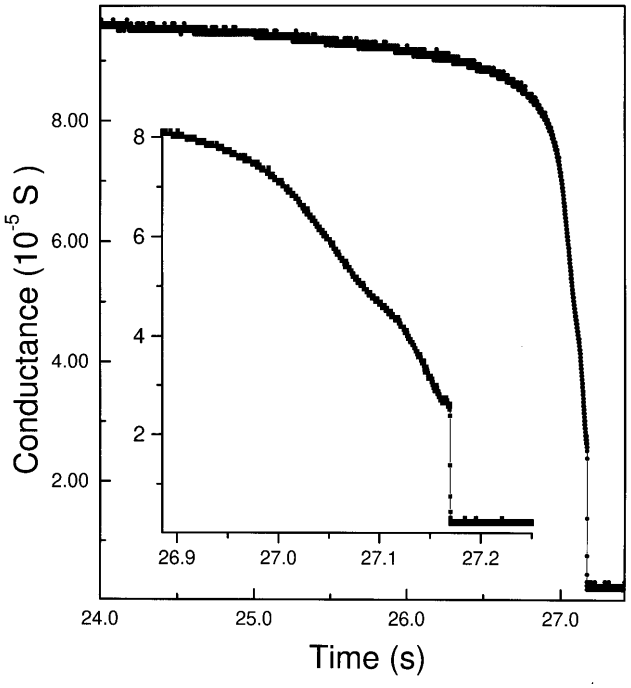

Fig. 14. Time dependence of the conductance through a 140-nm constriction following the application of a 2.5-V stress voltage

reaction to the area where J_e is highest and this leads to high spatial resolution. Conductance curves such as that shown in Fig. 14 also show kinks and a step near the end of the barrier formation process. We are currently working to elucidate the detailed mechanism of the current oxidation process and use it to fabricate model devices.

4 Conclusions

We have discussed two different ways of inducing the controlled oxidation of silicon and metals on the nanometer scale. In the first approach, the electric field of a conducting AFM tip was used to induce oxidation. The measurement of weak ionic currents of the correct magnitude and time dependence proves the electrochemical nature of the oxidation process. We have also measured the kinetics of this process and found it to be sensitively dependent on the applied bias and the resulting electric field strength. Moreover, we found that the oxidation rate shows self-limiting behavior with the rate decreasing exponentially with increasing oxide thickness. We interpreted this behavior as arising from the development of stress during oxidation, which in turn leads to a thickness-dependent activation energy. The ultimate oxide thickness that can be grown in a controlled manner by this approach is limited by dielectric breakdown events that can occur at biases > 10 V. The lateral resolution of the process was shown to be primarily determined by the defocusing of the electric field of the AFM tip by a condensed film of water that forms near its apex. The extent of this film and the resulting field defocusing depend on the ambient humidity and the hydrophilicity of the growing oxide.

We have also discovered that controlled local oxide growth on the nanometer scale can be induced by the current flowing through a conductor. By generating constrictions on a metallic conductor by using the AFM-induced oxidation process described above, current densities in the range of 10^6–10^7 A/cm^2 can easily be generated. We found that, under these conditions, thin oxide barriers soon grow and bridge the constrictions. By measuring the current as a function of temperature we determined the tunneling barrier height and found it to be that of a Ti/TiO_x barrier. The barrier width can be controlled by varying the applied stress voltage. The detailed mechanism of this oxidation process has not been elucidated yet. It is clear, however, that it involves the action of the electric current and is promoted by high current densities. The current and the associated electric field induce atomic rearrangements particularly at the metal grain boundaries. Nanocracks formed at these boundaries allow oxidants from the ambient to reach to the interior of the film. At the same time, the high current densities lead to Joule and local heating and thus promote chemistry.

Acknowledgements. We would like to acknowledge the valuable contributions of Mr. Bruce Ek. T.H. acknowledges financial support by the Alexander von Humboldt foundation and the Max-Planck-Society.

References

1. C.A. Quate: In *Highlights in Condensed Matter Physics and Future Prospects*, L. Esaki (Ed.) (Plenum Press, New York 1991)
2. Ph. Avouris (Ed.): *Atomic and Nanometer Scale Modification of Materials: Fundamentals and Applications* (Kluwer Academic Publishers, Dordrecht 1993)

3. V.T. Binh, N. Garcia, K. Dransfeld (Eds.): *Nanosources and Manipulation of Atoms under High Fields and Temperatures* (Kluwer Academic Publishers, Dordrecht 1993)
4. J.A. Dagata, J. Schneir, H.H. Harary, C.J. Evans, M.T. Postek, J. Bennett: Appl. Phys. Lett. **56**, 2001 (1990)
5. H.C. Day, D.R. Allee: Appl. Phys. Lett. **62**, 2691 (1993)
6. M. Yasutake, Y. Ejiri, T. Hattori: Jpn. J. Appl. Phys. Lett. **32**, L1021 (1993)
7. E.S. Snow, P.M. Campbell: Appl. Phys. Lett. **64**, 1932 (1994)
8. T. Hattori, Y. Ejiri, K. Saito, M. Yasutake: J. Vac. Sci. Technol. A **12**, 2586 (1994)
9. A.E. Gordon, R.T. Fayfield, D.D. Litfin, T.K. Higman: J. Vac. Sci. Technol. B **13**, 2805 (1995)
10. T. Teuschler, K. Mahr, S. Miyazaki, M. Hundhausen, L. Ley: Appl. Phys. Lett. **67**, 3144 (1995)
11. H. Sugimura, T. Uchida, N. Kitamura, H. Masuhara: J. Phys. Chem. **98**, 4352 (1994)
12. S.C. Minne, H.T. Soh, Ph. Flueckiger, C.F. Quate: Appl. Phys. Lett. **66**, 703 (1995)
13. E.S. Snow, P.M. Campbell: Science **270**, 1639 (1995)
14. K. Matsumoto, S. Takahashi, M. Ishii, M. Hoshi, A. Kurokawa, S. Ichimura, A. Ando: Jpn. J. Appl. Phys. **34**, 1387 (1995)
15. Ph. Avouris et al.: In *The Physics of Semiconductors*, Vol. 1, pp. 51-58, M. Scheffler, R. Zimmermann (Eds.) (World Scientific, Singapore, 1996)
16. Ph. Avouris, T. Hertel, R. Martel: Appl. Phys. Lett., **71**, 285 (1997)
17. N. Cabrera, N.F. Mott: Rep. Prog. Phys. **12**, 163 (1949)
18. H.Z. Massoud, J.D. Plummer, E.A. Irene: J. Electrochem. Soc. **132**, 2685 (1985)
19. N.F. Mott: Philos. Mag. B **55**, 117 (1987)
20. N.F. Mott, S. Rigo, F. Rochet, A.M. Stoneham: Philos. Mag. B **60**, 189 (1989)
21. B. Kao, J.P. McVittie, W.D. Nix, K.C. Saraswat: IEEE Trans. Electron. Dev. **35**, 25 (1988)
22. G.F. Cerofolini, G. La Bruna, L. Meda: Mater. Sci. Eng., B **36**, 104 (1996)
23. D. Goldfaber-Gordon, M.S. Montemerlo, J.C. Love, G.J. Opiteck, J.C. Ellenbogen: Proc. IEEE, **85**, 521 (1997)
24. T.C. Shen et al.: Science **268**, 1590 (1995); Ph. Avouris et al.: Surf. Sci. **363**, 368 (1996)
25. A. Christou (Ed.): *Electromigration and Electronic Device Degradation* (Wiley-Interscience, New York 1994)